Hyperfine structure of the B^{3}Π_{1} state and predictions of optical cycling behavior in the X→B transition of TlF

E. B. Norrgard, E. R. Edwards, D. J. McCarron, M. H. Steinecker, D. DeMille, Shah Saad Alam, S. K. Peck, N. S. Wadia, and L. R. Hunter

Hyperfine Structure of the $B^3\Pi_1$ State and Predictions of Optical Cycling Behavior in the $X \to B$ transition of TlF

E. B. Norrgard,* E. R. Edwards, D. J. McCarron, M. H. Steinecker, and D. DeMille†

Department of Physics, Yale University, P.O. Box 208120, New Haven, Connecticut 06520, USA

Shah Saad Alam, S. K. Peck, N. S. Wadia, and L. R. Hunter‡

Physics Department, Amherst College, Amherst, Massachusetts 01002, USA

The rotational and hyperfine spectrum of the $X^1\Sigma^+ \to B^3\Pi_1$ transition in TlF molecules was measured using laser-induced fluorescence from both a thermal and a cryogenic molecular beam. Rotational and hyperfine constants for the B state are obtained. The large magnetic hyperfine interaction of the Tl nuclear spin leads to significant mixing of the lowest B state rotational levels. Updated, more precise measurements of the $B \to X$ vibrational branching fractions are also presented. The combined rovibrational branching fractions allow for the prediction of the number of photons that can be scattered in a given TlF optical cycling scheme.

I. INTRODUCTION

The $X^1\Sigma^+$ state of thallium monofluoride (TlF) has long been a platform for precision measurements of parity- and time-reversal symmetry violation [1–3], with high potential for discovery of new physics [4]. In particular, the high mass of Tl coupled with the high polarizability of the molecule make this system ideal for measuring the Schiff moment of the Tl nucleus [5].

Optical cycling [6] is a potentially powerful tool for enhancing the signal in a symmetry violation measurement. Unit-efficiency detection of the internal state is possible when the number of photons scattered per molecule exceeds the reciprocal of the total light collection efficiency (geometric and detector efficiencies). Optical cycling also allows for the application of large optical forces, which can be useful for precision measurements. Transverse cooling can decrease beam divergence (and increase downstream flux) [7], and longitudinal slowing and trapping can increase effective interaction times [8], leading to improved energy resolution.

Optical cycling requires the ability to optically couple a subspace of ground and excited states, such that the excited states rarely decay to uncoupled ground states. Recently, we proposed the TlF $X^1\Sigma^+(v_g = 0) \to B^3\Pi_1(v_e = 0)$ transition (where v_g (v_e) is the ground (excited) state vibrational quantum number) as a candidate for optical cycling and laser cooling [9], as this transition has a sufficiently short excited state lifetime ($\tau = 99\,\text{ns}$) and favorable vibrational branching fractions to form a quasi-closed optical cycle. In TlF, the $B^3\Pi_1$ state was expected to have resolved – and potentially very large – hyperfine (HF) structure [9]. The HF interaction in the excited state can lead to mixing of rotational states with different quantum numbers J; this in turn can break the usual

rotational selection rules, leading to branching to additional ground rotational levels which must be coupled to the optical cycle. Hence, it is crucial to characterize the rotational and HF structure of the excited state to understand and control rotational branching.

High-resolution microwave spectroscopy [10] has provided a detailed and precise understanding of the X state HF and rotational energies. Low-resolution spectroscopy with a pulsed UV laser by Wolf and Tiemann [11] allowed for determination of rovibrational energies of the $B^3\Pi_1$ state. In this paper, we present high-resolution laser spectroscopy of the $X^1\Sigma^+(v_g = 0) \to B^3\Pi_1(v_e = 0)$ transition. We clearly identify rotational lines associated with $B^3\Pi_1(v_e = 0)$ states from $J = 1 - 70$. The B state HF structure is fully resolved for $J \lesssim 51$ and is fit to a standard Hamiltonian to determine the parameters describing the HF interaction. These data allow a full characterization of the HF structure in the B state, including effects of HF-induced rotational state mixing. In addition, we present improved vibrational branching measurements from $v_e = 0$. Together, these data are used to quantitatively predict the number of photons that may be scattered on the $X^1\Sigma^+ \to B^3\Pi_1$ transition of TlF for various cycling schemes.

II. EXPERIMENTAL DETAILS

To allow access to and identification of a large range of rotational states, we make observations using both a thermal beam source and a cryogenic buffer gas beam source. The thermal oven source is the same as in Ref. [9]. It is described in brief here. The measurements are made in a stainless steel molecular beam apparatus maintained at a pressure of about 10^{-6} Torr. The beam itself is created by heating a stainless steel oven containing TlF to temperatures of 688-733 K. The beam emerges from the oven through four ceramic tubes. The tubes precollimate the beam, which is then further collimated by an aperture located about 30 cm from the oven.

The cryogenic buffer gas beam source is nearly identi-

cal to that of [12]. A solid target is made by melting TlF powder in a copper crucible under vacuum. The crucible is mounted inside a copper cell and held at roughly $4\,\mathrm{K}$ by a pulse tube refrigerator. TlF molecules are produced by laser ablation of the target with $10\,\mathrm{ns}$, $25\,\mathrm{mJ}$ pulses of $1064\,\mathrm{nm}$ light, and are extracted from the cell by a flow of typically $5\,\mathrm{sccm}$ of cryogenic helium buffer gas. The molecular beam then propagates through a region held at roughly $10^{-7}\,\mathrm{Torr}$.

The $X(0) \to B(0)$ transition occurs at wavelength $271.7\,\mathrm{nm}$. A CW, single-frequency, tunable $1087\,\mathrm{nm}$ fiber laser is frequency doubled twice to produce roughly $20\,\mathrm{mW}$ of CW $271.7\,\mathrm{nm}$ light, using commercial resonant bow-tie cavities. The fiber laser frequency is locked by monitoring its transmission through a scanning Fabry-Perot cavity; the Fabry-Perot cavity length is in turn stabilized by simultaneously monitoring the transmission of a frequency-stabilized helium-neon laser.

In both molecular beam setups, the $271.7\,\mathrm{nm}$ laser light is directed to intersect the molecular beam perpendicular to the direction of molecule motion. Laser-induced fluorescence is collected onto a photomultiplier tube (PMT) in photon counting mode. In the thermal source, the fluorescence is collimated, passed through an interference filter, and then spatially filtered and collected. In the cryogenic source, the fluorescence is transferred to the PMT by a light pipe, followed by an interference filter.

III. HYPERFINE AND ROTATION HAMILTONIAN

A. Quantum Numbers in the $X - B$ Spectrum

Thallium has two common isotopes, ^{203}Tl ($30\,\%$ natural abundance) and ^{205}Tl ($70\,\%$), both with nuclear spin $I_1 = 1/2$ [13]. Fluorine's only isotope is ^{19}F, also with nuclear spin $I_2 = 1/2$. We describe the B state of TlF using the Hund's case (c) basis and the coupling scheme:

$$\begin{aligned} \boldsymbol{F_1} &= \boldsymbol{J} + \boldsymbol{I_1}, \\ \boldsymbol{F} &= \boldsymbol{F_1} + \boldsymbol{I_2}, \end{aligned} \quad (1)$$

where J is the total angular momentum of the molecule less nuclear spin. Hence each rotational state with quantum number J has associated HF states with $F_1 = J \pm \frac{1}{2}$ and $F = J - 1$, J, J, and $J + 1$.

The Hund's case (c) basis kets $|c\rangle$ are:

$$|c\rangle = |J, \Omega, I_1, F_1, I_2, F, m_F, P\rangle . \quad (2)$$

Here, Ω is the projection of J on the internuclear axis, m_F is the projection of F in the lab frame, and $P = \pm 1$ is the state parity. Following the convention of Herzberg [14], we refer to states with $P = (-1)^J$ as e-parity and $P = (-1)^{J+1}$ as f-parity states. As described below, the large HF interactions in the B state mix neighboring rotational levels. We use rotational quantum number J to describe states in the basis of Eq. 2, and label energy

eigenstates in the case of large mixing by $\tilde{J}$ (i.e. $\tilde{J} = J$ in the absence of HF mixing). We denote the rotational quantum number in the ground state by J_g.

B. Magnetic Hyperfine

The largest HF effect is expected to be due to the magnetic HF interaction, described by the Hamiltonian H_{mhf}:

$$H_{\mathrm{mhf}} = a\boldsymbol{I} \cdot \boldsymbol{L} + b\boldsymbol{I} \cdot \boldsymbol{S} + cI_z S_z, \quad (3)$$

where $I = I_1$ or I_2; L is the total electron orbital angular momentum; and S is the total electron spin. The lower-case subscript corresponds to coordinates in the molecule fixed-frame, with $\hat{z}$ along the internuclear axis. Terms involving $I_\pm L_\mp$ and $I_\pm S_\mp$ are negligible, as they only couple to other electronic states which differ in energy from the $B^3\Pi_1$ state by much more than the HF interaction [15]. Ignoring such terms, we may write the effective Hamiltonian in the form

$$\begin{aligned} H_{\mathrm{mhf}}^{\mathrm{eff}} &= \left(aL_z + (b+c)S_z\right)I_z, \\ &= h_\Omega I_z. \end{aligned} \quad (4)$$

Here, $h_\Omega = a\langle L_z \rangle + (b+c)\langle S_z \rangle$, where $\langle \rangle$ corresponds to the expectation value of the operators in the electronic state of interest. For $I = I_1$,

$$\begin{aligned} &\langle J, \Omega, F_1, F, m | H_{\mathrm{mhf}}(\mathrm{Tl}) | J', \Omega', F_1', F, m \rangle \\ &= h_1(\mathrm{Tl})(-1)^{J+J'+F_1+I_1-\Omega} \delta_{F_1, F_1'} \\ &\quad \times [(2J+1)(2J'+1)I_1(I_1+1)(2I_1+1)]^{1/2} \\ &\quad \times \begin{Bmatrix} I_1 & J' & F_1 \\ J & I_1 & 1 \end{Bmatrix} \begin{pmatrix} J & 1 & J' \\ -\Omega & 0 & \Omega' \end{pmatrix}. \end{aligned} \quad (5)$$

Similarly for $I = I_2$,

$$\begin{aligned} &\langle J, \Omega, F_1, F, m | H_{\mathrm{mhf}}(\mathrm{F}) | J', \Omega', F_1', F, m \rangle \\ &= h_1(\mathrm{F})(-1)^{2F_1'+F+2J-\Omega+1+I_1+I_2} \\ &\quad \times \begin{Bmatrix} I_2 & F_1' & F \\ F_1 & I_2 & 1 \end{Bmatrix} \begin{Bmatrix} J' & F_1' & I_1 \\ F_1 & J & 1 \end{Bmatrix} \begin{pmatrix} J & 1 & J' \\ -\Omega & 0 & \Omega' \end{pmatrix} \\ &\quad \times [(2F_1+1)(2F_1'+1)(2J+1)(2J'+1) \\ &\quad \times I_2(I_2+1)(2I_2+1)]^{1/2}. \end{aligned} \quad (6)$$

C. Nuclear Spin-Rotation

The effective nuclear spin-rotation Hamiltonian is of the form $H_{\mathrm{nsr}} = c_I(\boldsymbol{I} \cdot \boldsymbol{J})$, where again $I = I_1$ or I_2. This arises from two physical mechanisms. The first is the coupling of the rotational motion of the nuclei to the nuclear spin magnetic moments. For an electronic state which is not strongly perturbed by other nearby states, this contribution dominates, and c_I is quite small (for example, $c_I(\mathrm{Tl}) = 126.03\,\mathrm{kHz}$ and $c_I(\mathrm{F}) = 17.89\,\mathrm{kHz}$ in the

$X^1\Sigma$ state in TlF [1]). The second contribution arises from second-order rotational coupling to other electronic states [16]. This contribution likely dominates in the B state, where levels with $^3\Delta$ and $^3\Sigma$ character are predicted to lie near in energy [15]. In such a situation, c_I can be significantly larger than when the main contribution comes from the first mechanism; for example, in ^{195}PtF, $c_I(\mathrm{Pt}) = 3.11\,\mathrm{MHz}$ [16].

The nuclear spin-rotation matrix elements can be written as follows. For $I = I_1$:

$$\langle J, \Omega, F_1, F, m | H_{\mathrm{nsr}}(\mathrm{Tl}) | J', \Omega', F_1', F, m \rangle$$
$$= c_I(\mathrm{Tl})(-1)^{J+F_1+I_1} \delta_{F_1, F_1'} \delta_{J,J'} \begin{Bmatrix} I_1 & J & F_1 \\ J & I_1 & 1 \end{Bmatrix} \quad (7)$$
$$\times [(J(J+1)(2J+1)I_1(I_1+1)(2I_1)+1)]^{1/2}.$$

For $I = I_2$:

$$\langle J, \Omega, F_1, F, m | H_{\mathrm{nsr}}(\mathrm{F}) | J', \Omega', F_1', F, m \rangle$$
$$= c_I(\mathrm{F})(-1)^{2F_1'+F+J+I_1+I_2+1} \delta_{J,J'}$$
$$\times \begin{Bmatrix} I_2 & F_1' & F \\ F_1 & I_2 & 1 \end{Bmatrix} \begin{Bmatrix} J' & F_1' & I_1 \\ F_1 & J & 1 \end{Bmatrix} \quad (8)$$
$$\times [(2F_1+1)(2F_1'+1)J(J+1)(2J+1)$$
$$\times I_2(I_2+1)(2I_2+1)]^{1/2}.$$

Because there are discrepancies in the literature about the explicit form of these HF matrix elements, we derive them in Appendix C.

D. Additional Terms

Equations 5 and 6 are only strictly valid for an isolated electronic level. Perturbations by a nearby level can lead to extra terms in the effective Hamiltonian with the J-dependence of centrifugal terms, modeled by substituting $h_1 \to h_1 + h_{1D}J(J+1)$ [17]. However, the diagonal matrix elements of the centrifugal magnetic HF and nuclear spin-rotation Hamiltonians are identical, and the effects of off-diagonal elements are too small to be discernable in our data. We choose to constrain $h_{1D} = 0$, and treat the fit constants $c_I(\mathrm{Tl})$ and $c_I(\mathrm{F})$ as empirical combinations of the two effects.

Rotational energy is modeled using the standard effective Hamiltonian H_{rot} [14]:

$$H_{\mathrm{rot}} = B_0 \boldsymbol{J}^2 - D_0 \boldsymbol{J}^4 + H_0 \boldsymbol{J}^6 \ldots, \quad (9)$$

with diagonal matrix elements

$$\langle J, \Omega, F_1, F, m | H_{\mathrm{rot}}(\mathrm{F}) | J, \Omega, F_1, F, m \rangle$$
$$= B_0 J(J+1) - D_0(J(J+1))^2 + H_0(J(J+1))^3 \ldots \quad (10)$$

The B state HF/rotation structure is expected to depend on the isotopologue and the e/f parity. We therefore fit the parity states and each Tl isotope separately. This is equivalent to the analysis of Ref. [16], which used the substitution $h_1 \to h_1 \pm h_{1q}$ and and $c_I \to c_I \pm c_{Iq}$, with the upper (lower) sign used for the e- (f-) parity states.

IV. OBSERVED SPECTRAL FEATURES

A. Line Identification

The HF structure of the ground $X^1\Sigma^+$ state is unresolved ($\sim 100\,\mathrm{kHz}$) in our optical spectra. In the excited $B^3\Pi_1$ state, we expect 8 well-split isotope/HF sublevels for each rotational level $\tilde{J}$ and parity P, corresponding to $F_1 = \tilde{J} \pm \frac{1}{2}$, $F = F_1 \pm \frac{1}{2}$, and the two Tl isotopes. We label the 7 splittings between the 8 lines as $a, b, \ldots g$ as shown in Fig. 1. In most cases, we easily identify lines associated with the two isotopologues, since their intensities are proportional to the isotopic abundance: we associate splittings a, b, c with ^{205}Tl; e, f, g with ^{203}Tl; and d with the gap between the isotopologues. For a given isotopologue, the largest splitting (associated with the Tl nuclear spin projection) is b or f. The doublets separated by a, c (e, g) then correspond to the ^{19}F nuclear spin projection for ^{205}TlF (^{203}TlF). As described in Section IV B below, in $\tilde{J} = 1$ only, the separation of the levels due to the Tl spin projection is larger than the isotope shift; we use the convention of labeling the splitting between the highest ^{205}TlF HF level and the lowest ^{203}TlF HF level as d, and thus $d < 0$ for transitions to $\tilde{J} = 1$.

The R and P branch transitions are spectroscopically isolated and hence relatively easy to identify for $\tilde{J} > 1$. For these states, 8-line multiplets similar to that displayed in Fig. 1 are found approximately centered on the locations predicted from the Dunham coefficients of Tiemann [18]. Our measured splittings for the various values of e-parity excited states are listed in Table I.

Assignment of the Q branch transitions is more challenging. Due to the near equality of the rotational constants of the X and B states, the Q branch transitions are generally not clearly separated. All of the lines between Q_1 and Q_{60} (approximately 480 individual HF transitions) are contained in a frequency range of about 21 GHz (see Appendix D). We initially identified many of the Q branch multiplets for Q_{11}–Q_{34} using rotational constants B_0, D_0, and H_0 from Tiemann [18], then fine-tuned these parameters to obtain good agreement with all the identifiable Q branch lines (Q_{11}–Q_{68}). Because of their lower abundance and correspondingly smaller signals, no similar identification was possible for the majority of the ^{203}TlF Q branch lines. Assuming the same rotational constants (scaled for reduced mass and including an isotopic offset), we have made some tentative assignments of ^{203}TlF Q_{60}–Q_{71}.

The HF splitting is larger than the separation of Q branch transitions for Q_1–Q_{10}, and clear identification of the lines again becomes problematic. Ignoring the splittings which are obscured by overlapping Q branch lines eliminates nearly all Q_1–Q_{10} data (except Q_4 and Q_9). However, superposing the data taken in this spectral region from both the thermal beam and the cryogenic beam provides additional information and leads to the tentative assignments shown in Fig. 2a. The resulting splittings
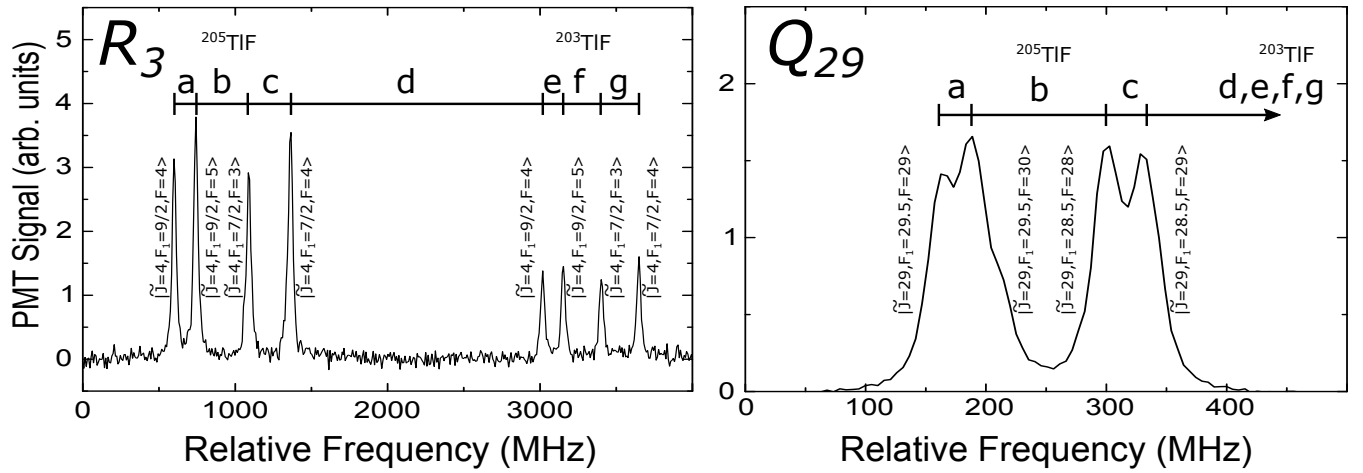
FIG. 1. PMT signal vs laser frequency in the thermal source. The scan over the R_3 lines (left) shows the labeling scheme for observed isotope/HF splittings used in the P, Q and R branch lines. The basic pattern of HF structure repeats with decreasing splittings as $\tilde{J}$ increases, as observed in the Q_{29} line (right).

$\tilde{J}$	R	a	b	c	d	e	f	g	P	a	b	c	d	e	f	g
21	20	37	354	42												
...																
16	15	50	303	60												
...																
11	10	66	274	83												
...																
9	8	*91*	*272*	*99*												
8	7	*88*	*270*	*110*	*2203*	*80*	*224*	*113*								
7	6	*93*	*269*	*128*	*2157*	*93*	*224*	*128*								
6	5	105	297	153	2108	113	231	150								
5	4	121	304	189	2050	125	247	185								
4	3	147	343	255	1909	147	266	249	5	*142*	*379*	*250*	*1813*	*151*	*254*	*247*
3	2	178	391	341	1735	179	302	335	4	175	388	341	1646	188	309	332
2	1	227	463	580	1378	229	326	579	3	256	*475*	562	*1340*	225	*315*	*560*
1	0	*548*	*13524*	*304*				*289*	2	*545*	*13523*	*305*	*-11711*	*582*	*13431*	*309*

TABLE I. Observed splittings of e-parity levels (MHz). Regular (italic) type indicates splittings measured in the thermal (cryogenic) beam.

for f-parity excited states are listed in Table II.

We now discuss a number of unusual features in the B state HF structure. Many of these observations are attributed to an unusually large value of $h_1(\text{Tl})$ (found to be $\approx 29\,\text{GHz}$), which we believe may be the largest observed HF interaction in any diatomic molecule.

B. Large Hyperfine Splitting for $\tilde{J} = 1$

The large value of $h_1(\text{Tl})$ is best illustrated by the enormous b splitting in $\tilde{J} = 1$ (Fig. 2b). While the HF structure of $\tilde{J} = 1$ covers $\sim 13\,\text{GHz}$, all higher Q branch lines to $\tilde{J} \geq 2$ observable in the cryogenic source (Q_2 to roughly Q_8) are contained in only roughly $2\,\text{GHz}$. The large splitting in $\tilde{J} = 1$ means two of the four R_0 lines are actually lower in frequency than Q_2.

C. J-mixing and "Extra" Lines

In addition to the expected P, Q and R branch lines, we observe additional quartets of lines near several low P and R branch lines (Fig. 3). These are assigned as nominal $\Delta J = -2, +2$ transitions (O and S branch, respectively). The presence of these lines is an indication that the B state rotational levels are strongly mixed by the magnetic HF interaction. If $|h_1(\text{Tl})| \gg |h_1(\text{F})|$, as expected since HF structure is enhanced in heavier species, then this J-mixing is only significant between states with the same values of F_1 *and* F. The eigenstates can be written in the form

$$\left| \tilde{J}, F_1 = \tilde{J} + \frac{1}{2} \right\rangle = \alpha_{F_1} \left| J = \tilde{J} \right\rangle + \beta_{F_1} \left| J = \tilde{J} + 1 \right\rangle,$$

$$\left| \tilde{J} + 1, F_1 = \tilde{J} + \frac{1}{2} \right\rangle = \beta_{F_1} \left| J = \tilde{J} \right\rangle - \alpha_{F_1} \left| J = \tilde{J} + 1 \right\rangle.$$
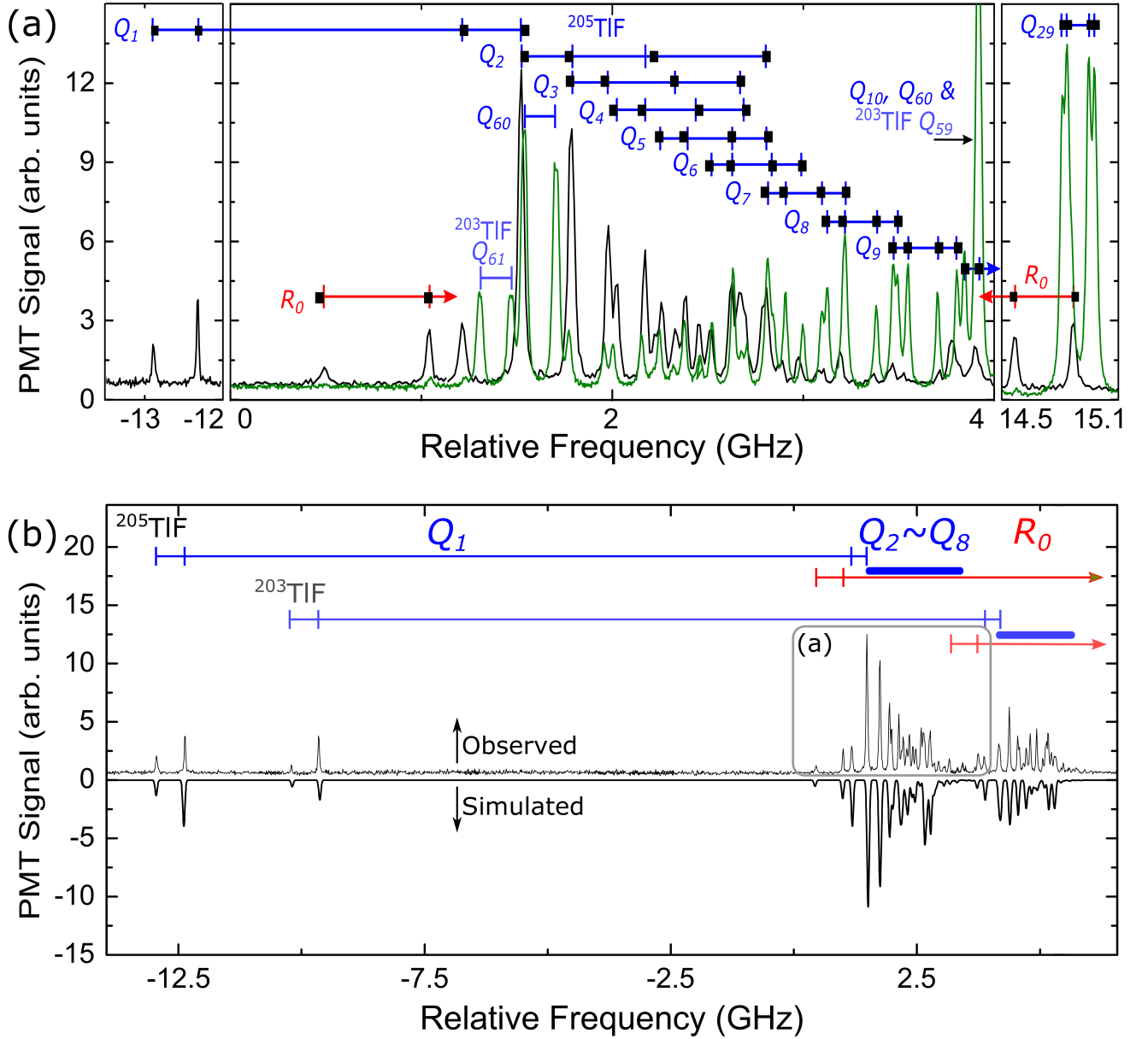
(11)

FIG. 2. (Color online) PMT signal vs laser frequency. (a) PMT signals from the thermal (green) and cryogenic (black) beams. Comparison of the two spectra allow for tentative ^{205}TlF line assignments (blue ticked lines) despite overlap of several low Q branch lines and R_0 (red ticked lines). These assignments are in excellent agreement with the line centers predicted by the best-fit Hamiltonian (black squares), even out to large values of $\tilde{J}$, such as Q_{29}. The small variations of the line locations observed in the two sources is likely because the frequency data in the cryogenic source was not corrected for nonlinearities in the Fabry-Perot cavity scan. (b) A scan over the Q branches and part of R_0 in the cryogenic source. Grey box approximates the frequency range of the central frame of panel (a). While the HF structure of $\tilde{J} = 1$ covers ~ 13 GHz, all higher Q branch lines observable in the cryogenic source (Q_2 to roughly Q_8) are contained in only ~ 2 GHz (solid blue bar). The large splitting in $\tilde{J} = 1$ means that for each Tl isotope, the lower two of the four R_0 lines are actually lower in frequency than the upper two Q_1 lines. Below the observed spectrum is plotted an inverted simulated spectrum calculated from the fit Hamiltonian values in Table III. The full $1/e^2$ linewidth is set to the observed Doppler limited width of 31 MHz. The simulated intensities are determined up to an overall scaling factor by the calculated relative line strengths S [19], isotopic abundance, and an assumed Boltzmann rotational distribution with temperature T. A fit to 10 lines representing $J_g = 0$–4 gives $T = 3.6^{+1.0}_{-0.8}$ K. In the simulated spectrum, ^{203}TlF Q branch lines are produced using a fitted isotope shift and the ^{205}TlF f-parity HF parameters, with $h_1(^{203}\text{Tl}) = h_1(^{205}\text{Tl})g_{203}/g_{205}$.

J̃	Q	a	b	c	d	e	f	g	O	h	i	j	S	k	l	m
70	70						177									
69	69						176									
68	68		179				171									
67	67						173									
66	66		175				168									
65	65		176				168									
64	64		175				167									
63	63		184				166									
62	62		177				165									
61	61		170				164									
60	60		168													
59	59		157													
...																
51	51	17	139	17												
...																
34	34	27	111	26												
...																
29	29	26	114	26												
...																
27	27	25	113	32												
...																
25	25	30	108	29												
...																
23	23	37	110	42												
...																
20	20	36	110	45												
...																
17	17	46	115	50												
16	16	48	115	54												
...																
14	14	56	121	64												
13	13	59	133	70												
12	12	63	131	76												
11	11	68	140	80												
10	10	**74**	**157**	**78**												
9	9	75	155	100												
8	8	**90**	**164**	111												
7	7	**93**	194	**116**												
6	6	**107**	**221**	150										4			154
5	5	**129**	**255**	**179**										3	*180*	*2430*	*184*
4	4	152	302	245										2	*244*	*2355*	*235*
3	3	**182**	372	344										1	*367*	*2229*	*347*
2	2	**233**	472	**568**										0	*561*	*1948*	*578*
1	1	571	13522	**316**	*-11361*	*553*			3	*312*	*2269*	*309*				

TABLE II. Observed splittings of f-parity levels (MHz). Regular (italic) type indicates splittings measured in the thermal (cryogenic) beam. Bold indicates splittings of tentative line assignments based on comparisons of overlapping lines present in both beams.

Note that $\left|\tilde{J}=1, F_1=1/2, F=0,1\right\rangle$ is a special case which does not experience J-mixing. For all other excited states, J-mixing leads to electric dipole-allowed O and S branch transitions. Because the rotational constants of the X and B states are nearly identical, the O_J lines appear very close to P_{2J-1}, and the S_J lines appear very close to R_{2J+2}. We label the splittings as h, i, j for the O-branch and k, l, m for the S-branch (see Fig. 3).

The P and R branches target the excited state e-parity levels. We check our line assignments by comparing splittings in R_J with those in P_{J+2}, which share a common excited state and thus should have the same observed HF splittings. The O, Q, and S branches target the excited state f-parity levels. The Q_J branch HF structure must be compared to both O_{J+2} and S_{J-2} branches, as these lines address only one value of F_1 in the excited state due to the selection rule $\Delta F_1 = \pm 1, 0$.

As an aside, we note that the ^{19}F magnetic HF interaction mixes states with the same F_1, and thus it is in principle possible to drive electric dipole transitions with $\Delta J = -3, +3$, which we call the N and T branches, respectively. For nearly equal ground and excited state rotational constants, we expect two T_J lines – one for each isotope, and split by $d + e + f + g$ for R_{J+2} – to appear very close to R_{3J+5} (and similarly, N_J lines near P_{3J-3}). Because the majority of the molecules produced in our cryogenic buffer gas beam source are in $J_g = 0, 1$, we searched for T_0 and T_1 lines around R_5 and R_8, respectively. However, we failed to detect any such transitions.
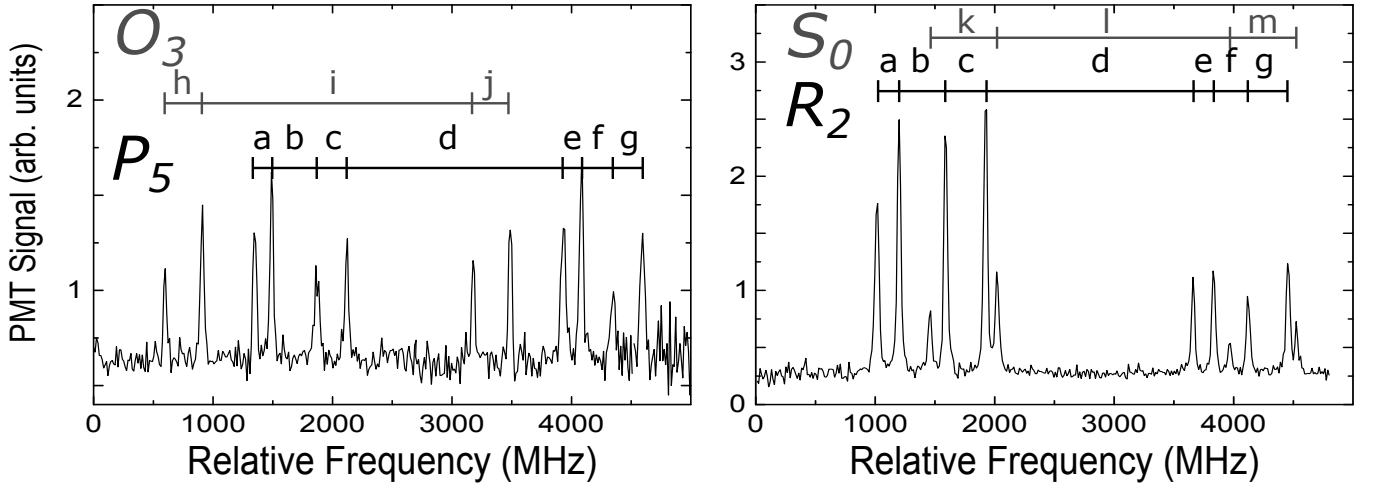
FIG. 3. PMT signal vs laser frequency in the cryogenic source. Examples of additional lines assigned to O branch (left) and S branch (right) transitions.

D. Inverted F_1 Doublet for $\tilde{J} \geq 2$

By examining the patterns in the data we can infer the ordering of the energy levels within different quartets of lines. The k splitting of the S branch lines is consistent with the c splitting (upper fluorine doublet splitting) of the Q branch, indicating that $\left|\tilde{J}, F_1 = \tilde{J} - \frac{1}{2}\right\rangle$ lies higher in energy than $\left|\tilde{J}, F_1 = \tilde{J} + \frac{1}{2}\right\rangle$ for all observed S branch lines, corresponding to $\tilde{J} = 2$–5. However, the h splitting for O_3 is also consistent with the c splitting of Q_1. Combined with the fact that $a > c$ for all lines connected to $\tilde{J} = 1$, but $a < c$ for $\tilde{J} \geq 2$, we conclude that the ordering of F_1 levels is regular only in $\tilde{J} = 1$, and inverted for $\tilde{J} \geq 2$. Also of note is that the b splitting is $\sim 29\times$ larger in $\tilde{J} = 1$ than in $\tilde{J} = 2$. Naively, the J-scaling of diagonal matrix elements of $H_{\mathrm{mhf}}^{\mathrm{eff}}$ (Eq. 5) would have led us to expect the b splitting to only be $\sim 2\times$ larger in $\tilde{J} = 1$ than in $\tilde{J} = 2$.

These peculiar features can be explained by an exceptionally large value of $h_1(\mathrm{Tl})$. Consider a simplified system where only $H_{\mathrm{mhf}}(\mathrm{Tl})$ (Eq. 4) and $H_{\mathrm{rot}} = B\boldsymbol{J}^2$ are present. In the basis of states $|J = F_1 \pm 1/2, F_1\rangle$ with $F_1 \geq 3/2$, the interaction is characterized by the 2×2 Hamiltonian

$$H_{2\times2} = \begin{pmatrix} \frac{4F_1^2-1}{4}B + h & \frac{\sqrt{4F_1^2+4F_1-3}}{2(2F_1+1)}h \\ \frac{\sqrt{4F_1^2+4F_1-3}}{2(2F_1+1)}h & \frac{(2F_1+3)(2F_1+1)}{4}B - h \end{pmatrix}. \quad (12)$$

By diagonalizing $H_{2\times2}$, we find the energy $E_{F_1}^\pm$ of eigenstate $\left|\tilde{J} = F_1 \pm 1/2, F_1\right\rangle$ is given by

$$E_{F_1}^\pm = B\left(F_1+\frac{1}{2}\right)^2 \pm \frac{1}{2}\sqrt{B^2(2F_1+1)^2 - 4Bh + h^2}. \quad (13)$$

The energy difference between states $\left|\tilde{J}, F_1 = \tilde{J} \pm 1/2\right\rangle$
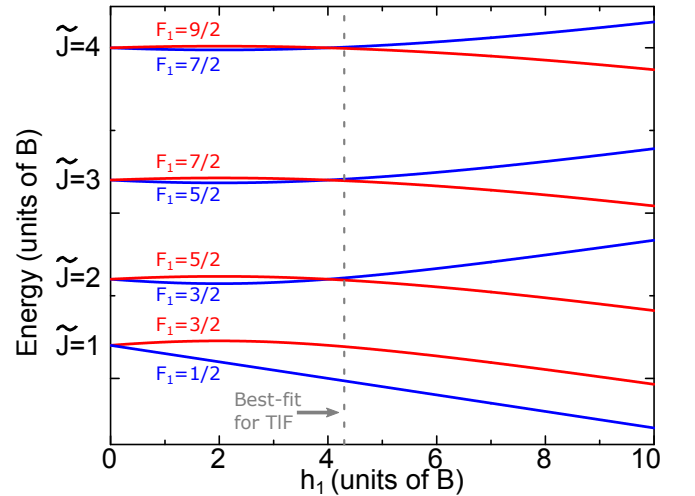

FIG. 4. (Color Online) Eigenvalues of model Hamiltonian containing only rotation and magnetic HF interaction of a single nuclear spin $I = 1/2$.

vanishes for $\tilde{J} \geq 2$ when $h = 4B$ (see Fig. 4). The energy ordering of the F_1 doublets reverses for $h_1 > 4B$ for all $\tilde{J} \geq 2$, but not for $\tilde{J} = 1$. For $h_1 \simeq 4B$, the splitting of $\tilde{J} = 1$ is much greater than that of all other states. These features are consistent with our observations and our fit value $h_1(\mathrm{Tl})/B_0 = 4.3$.

E. Fitting

The best-fit values for the rotational and HF parameters are provided in Table III. The B state rotational parameters are obtained by subtracting off the precisely-known X state rotational energy from the weighted cen-

	This Work			Ref. [18]			
	e-parity		f-parity	e-parity		f-parity	
Parameter	^{203}TlF	^{205}TlF	^{205}TlF	^{203}TlF	^{205}TlF	^{203}TlF	^{205}TlF
B_0	6694.42(19)	6689.09(16)	6686.667(26)	6694.5(11)	6688.9(11)	6694.3(11)	6688.7(11)
D_0			0.010869(27)	0.01089(14)	0.01088(14)	0.01098(14)	0.01096(14)
$H_0 \cdot 10^8$			-8.1(6)	-9.0(6)	-9.0(6)	-9.0(6)	-9.0(6)
h_1(Tl)	28516(5)	28793(5)	28802(4)				
h_1(F)	864(1)	859(1)	871(1)				
c_I(Tl)	-13.9(1)	-13.5(1)	-2.2(1)				

TABLE III. Fit rotational and HF parameters for the $B^3\Pi_1$ state of TlF. Numbers in parentheses are the 1σ confidence intervals. All values are in MHz. The root mean square deviation between our fitted and measured splittings is $< 8\,\mathrm{MHz}$ in all cases. The residual is $< 20\,\mathrm{MHz}$ for each fitted point, and tends to decrease with increasing $\tilde{J}$.

ter of the HF quartet for each isotope, then fitting to a polynomial in $\tilde{J}(\tilde{J}+1)$. For the f-parity, we perform a cubic fit to Q_{11}–Q_{60}. For the e-parity, we fit to R_1–R_8, and only the linear (B_0) term is statistically significant. The R_0 lines are excluded from the fit as they are observed to deviate strongly from the rotational progression as discussed above. The e-parity level B_0 constants are observed to match the expected scaling with molecular reduced mass μ: $^{203}B_0/^{205}B_0 = 1.00080(4)$, while $\mu_{205}/\mu_{203} = 1.00084$.

The HF fit parameters are obtained by diagonalizing the effective Hamiltonian $H = H_{\mathrm{rot}} + H_{\mathrm{mhf}}(\mathrm{Tl}) + H_{\mathrm{mhf}}(\mathrm{F}) + H_{\mathrm{nsr}}(\mathrm{Tl}) + H_{\mathrm{nsr}}(\mathrm{F})$ for each value of F. The HF parameters for the f- (e)-parity states were fit to the observed Q branch (average of the P and R branch) splitting, weighted by their assigned uncertainties. In all cases, we find $c_I(\mathrm{F})$ to be consistent with zero within an uncertainty of $0.1\,\mathrm{MHz}$.

The uncertainty in the splittings measured in the thermal beam is $3\,\mathrm{MHz}$. For the cryogenic beam data, the Fabry-Perot ramp was less linear, and we assign an uncertainty of $8\,\mathrm{MHz}$ to these splittings. We fit to the thermal beam data if available, and the cryogenic beam data when not. In the instances where lines were measured in both setups, the agreement is typically within $10\,\mathrm{MHz}$. As a check of our Q branch splitting assignments where one or both lines are degenerate with other Q branch lines (Table II bold data), a fit to the f-parity levels was performed excluding these data. However, this did not change the fit parameters within the assigned uncertainty. The excellent agreement between the data and the line centers predicted by the best-fit Hamiltonian (Fig. 2a) provides additional support for our tentative Q branch line assignments.

There is fair agreement between the ^{205}TlF and ^{203}TlF isotopologues on the value of the ^{19}F doublet splittings. The magnetic HF parameter $h_1(\mathrm{Tl})$ should be proportional to the nuclear g-factor g_N, and we find excellent agreement for e-parity: $h_1(^{203}\mathrm{Tl})/h_1(^{205}\mathrm{Tl}) = 0.9904(2)$, while $g_{203}/g_{205} = 0.990260$ [13]. Hyperfine anomalies are known to occur at the 10^{-4} level in neutral Tl atoms [20, 21], but is outside the precision of this study.

Finally, we extract the electronic isotope shift $\Delta\nu_{\mathrm{el}}(203-205)$ for the $X \to B$ transition [22]. By averaging the shift for each HF transition for all P and R branch lines and subtracting off the calculated rovibrational contributions, we find $\Delta\nu_{\mathrm{el}}(203-205) = +3309(9)\,\mathrm{MHz}$. Because we only measure two Tl isotopes, we are unable to deconvolve the mass- and field-shift contributions to this quantity [22].

V. OPTICAL CYCLING

A. Applications and Requirements

The ability to scatter many photons per molecule can be used for efficient detection and for application of optical forces. The number of optical cycles required before leaking into an uncoupled state depends on the application. For instance, simple state-selective detection of molecules in a beam often does not require a highly closed cycle. A typical laser-induced fluorescence setup can achieve overall detection efficiency for emitted photons (including detector quantum efficiency) of $\eta \sim 1$–10% [8]. Hence, to detect molecules with near-unit efficiency, we only require an optical cycling scheme closed to (very roughly) $1/\eta \sim 10$–100 cycles. Applying significant optical forces requires a more closed cycle: $\sim 10^3$ optical cycles are required to achieve transverse Doppler cooling of a molecular beam to milliKelvin temperatures [7], and $\sim 10^4$ optical cycles are needed to slow a molecular beam to a near stop [23] or to magneto-optically trap molecules [8].

In this section, we consider vibrational and rotational branching effects which can limit the number of photons scattered on a given spectral line of the TlF $X \to B$ transition. We denote the vibrational branching fraction $v_e \to v_g$ by $b_{v_e v_g}$, and rotational branching fraction $\tilde{J} \to J_g$ (irrespective of vibrational quantum number) by $r_{\tilde{J} J_g}$. We then propose a few optical cycling schemes which can be used in TlF for specific applications.

Nominal State Label	Calculated Admixture $\lvert J, F_1, F\rangle$				$r_{\tilde{J}\tilde{J}-2}$	$r_{\tilde{J}\tilde{J}}$	$r_{\tilde{J}\tilde{J}+2}$
$\lvert \tilde{J}=1, F_1=\frac{1}{2}, F=0\rangle$	$\lvert 1,\frac{1}{2},0\rangle$					1	
$\lvert \tilde{J}=1, F_1=\frac{1}{2}, F=1\rangle$	$+0.9996\,\lvert 1,\frac{1}{2},1\rangle$	$+0.0203\,\lvert 1,\frac{3}{2},1\rangle$	$-0.0180\,\lvert 2,\frac{3}{2},1\rangle$			0.9998	0.0002
$\lvert \tilde{J}=1, F_1=\frac{3}{2}, F=1\rangle$	$+0.0267\,\lvert 1,\frac{1}{2},1\rangle$	$-0.8518\,\lvert 1,\frac{3}{2},1\rangle$	$+0.5232\,\lvert 2,\frac{3}{2},1\rangle$			0.836	0.164
$\lvert \tilde{J}=2, F_1=\frac{3}{2}, F=1\rangle$	$+0.0048\,\lvert 1,\frac{1}{2},1\rangle$	$+0.5235\,\lvert 1,\frac{3}{2},1\rangle$	$+0.8520\,\lvert 2,\frac{3}{2},1\rangle$		0.091	0.909	
$\lvert \tilde{J}=1, F_1=\frac{3}{2}, F=2\rangle$	$+0.8482\,\lvert 1,\frac{3}{2},2\rangle$	$-0.5294\,\lvert 2,\frac{3}{2},2\rangle$	$-0.0138\,\lvert 2,\frac{5}{2},2\rangle$	$+0.0064\,\lvert 3,\frac{5}{2},2\rangle$		0.832	0.168
$\lvert \tilde{J}=2, F_1=\frac{5}{2}, F=2\rangle$	$-0.0104\,\lvert 1,\frac{3}{2},2\rangle$	$+0.0120\,\lvert 2,\frac{3}{2},2\rangle$	$-0.9353\,\lvert 2,\frac{5}{2},2\rangle$	$+0.3535\,\lvert 3,\frac{5}{2},2\rangle$	$4\cdot10^{-5}$	0.929	0.071
$\lvert \tilde{J}=2, F_1=\frac{3}{2}, F=2\rangle$	$+0.5295\,\lvert 1,\frac{3}{2},2\rangle$	$+0.8482\,\lvert 2,\frac{3}{2},2\rangle$	$+0.0011\,\lvert 2,\frac{5}{2},2\rangle$	$-0.0103\,\lvert 3,\frac{5}{2},2\rangle$	0.094	0.906	$6\cdot10^{-5}$
$\lvert \tilde{J}=3, F_1=\frac{5}{2}, F=2\rangle$	$+0.0040\,\lvert 1,\frac{3}{2},2\rangle$	$+0.0085\,\lvert 2,\frac{3}{2},2\rangle$	$+0.3536\,\lvert 2,\frac{5}{2},2\rangle$	$+0.9353\,\lvert 3,\frac{5}{2},2\rangle$	0.050	0.950	
$\lvert \tilde{J}=2, F_1=\frac{5}{2}, F=3\rangle$	$+0.9341\,\lvert 2,\frac{5}{2},3\rangle$	$-0.3568\,\lvert 3,\frac{5}{2},3\rangle$	$-0.0100\,\lvert 3,\frac{7}{2},3\rangle$	$+0.0032\,\lvert 4,\frac{7}{2},3\rangle$		0.927	0.073
$\lvert \tilde{J}=3, F_1=\frac{7}{2}, F=3\rangle$	$-0.0084\,\lvert 2,\frac{5}{2},3\rangle$	$+0.0074\,\lvert 3,\frac{5}{2},3\rangle$	$-0.9638\,\lvert 3,\frac{7}{2},3\rangle$	$+0.2665\,\lvert 4,\frac{7}{2},3\rangle$	$3\cdot10^{-5}$	0.961	0.039
$\lvert \tilde{J}=3, F_1=\frac{5}{2}, F=3\rangle$	$+0.3568\,\lvert 2,\frac{5}{2},3\rangle$	$+0.9341\,\lvert 3,\frac{5}{2},3\rangle$	$+0.0017\,\lvert 3,\frac{7}{2},3\rangle$	$-0.0084\,\lvert 4,\frac{7}{2},3\rangle$	0.051	0.949	$4\cdot10^{-5}$
$\lvert \tilde{J}=4, F_1=\frac{7}{2}, F=3\rangle$	$+0.0023\,\lvert 2,\frac{5}{2},3\rangle$	$+0.0073\,\lvert 3,\frac{5}{2},3\rangle$	$+0.2666\,\lvert 3,\frac{7}{2},3\rangle$	$+0.9638\,\lvert 4,\frac{7}{2},3\rangle$	0.031	0.970	

TABLE IV. Eigenstates and their rotational branching ratios $r_{\tilde{J}J_g}$ for $\lvert B(v_e=0), F=0-3, P=f\rangle$, calculated from the best-fit spectroscopic constants in Tables II and III for ^{205}TlF.

B. Rotational Branching

As discussed in Section IV C, HF interactions mix states of the same total angular momentum F. In Table IV, we present the eigenstates of $B(v_e=0)$ in the basis of Eq. 2 calculated from the best-fit spectroscopic constants in Table III. With the state admixture in hand, it is straightforward to calculate rotational branching fractions $r_{\tilde{J}J_g}$ using the line strengths S [19] for each excited basis state.

C. Vibrational Branching

Previous measurements of vibrational branching in TlF found favorable branching fractions $b_{v_e v_g}$ for cycling from the $B(v_e=0)$ state: $b_{00}=0.99$, $b_{01}<0.0002$, and $b_{02}=0.0110(6)$ [9]. Measurements of branching fractions to $v_g \geq 3$ were limited by experimental sensitivity and the availability of narrow bandpass interference filters at the needed wavelengths. Predicted values for these branching fractions using Morse and Rydberg-Klein-Rees (RKR) potentials, given in Table V, were uncertain at the level required to determine which of these transitions could be neglected during longitudinal cooling. Here we present precision measurements of b_{03}, b_{04}, b_{05}, and b_{06}.

Measurements of the branching fractions are done using a modified version of the thermal beam in order to take advantage of the better molecular beam intensity stability. Pulsed excitation is used, and fluorescence is only detected after the laser pulse, eliminating scattered-

$B(0) \to X(v_g)$		Morse	RKR	Measured
$v_g=0$	271.7 nm	0.9892(3)	0.989(2)	0.990(2)
$v_g=1$	275.3 nm	0.0003(2)	0.0005(3)	$25(7)\cdot10^{-5}$
$v_g=2$	278.8 nm	0.0104(2)	0.010(2)	0.010(2)
$v_g=3$	282.5 nm	0.00000(1)	<0.0003	$5(4)\cdot10^{-5}$
$v_g=4$	286.2 nm	0.00013(1)	<0.0002	$22(5)\cdot10^{-5}$
$v_g=5$	290.0 nm	0.00000(1)	<0.0003	$<2\cdot10^{-5}$
$v_g=6^+$	293.8 nm	$-$	<0.0002	$<2\cdot10^{-5}$

TABLE V. Predicted and measured values of the branching fractions b_{0v_g} in TlF. Calculations were done separately using the Morse potential and the RKR potential as models for the internuclear potential. Uncertainties in measured values given in parentheses represent 68 % Gaussian confidence intervals. In instances where a Gaussian confidence interval would contain unphysical negative values, a less than sign denotes a 68 % Feldman-Cousins confidence interval [24].

light backgrounds. The exciting laser light is produced by a pulsed dye laser with Coumarin 540A dye pumped by a 355 nm Nd:YAG laser with pulse duration of 10 ns and 10 Hz repetition rate. The output of the dye laser is frequency doubled to produce 271.7 nm light. Measurements are made with the broadband pulsed system tuned to the largest fluorescence signal that occurs, near a large pile-up of rotational transitions between Q_{30} and Q_{52} with a bandhead that occurs at about Q_{43}. Background measurements are made by tuning to the high frequency side of this bandhead where virtually no fluorescence occurs.
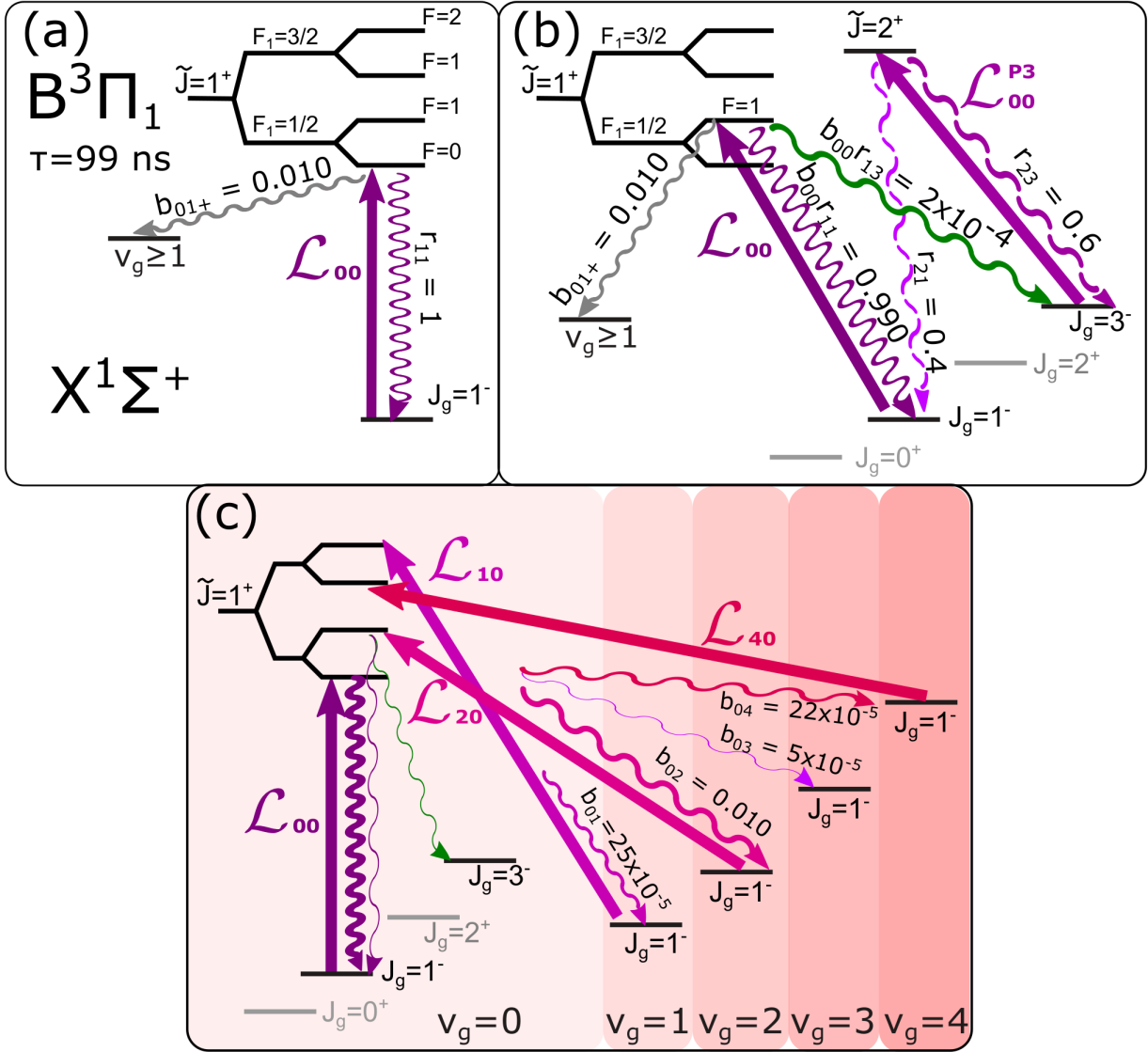
FIG. 5. (Color Online) Optical cycling schemes for TlF. Straight arrows with labels $\mathcal{L}_{v_g v_e}$ denote laser excitations $X^1\Sigma^+(v_g) \to B^3\Pi_1(v_e)$, wavy arrows denote spontaneous decay. Vibrational branching fractions are labeled $b_{v_e v_g}$, while rotational branching fractions for diagonal vibrational transitions are labeled as $r_{J'J}$. (a) Cycling with $\left|\tilde{J}=1, F_1=1/2, F=0, P=+\right\rangle$ as the excited state. (b) Cycling with $\left|\tilde{J}=1, F_1=1/2, F=1, P=+\right\rangle$ as the excited state. Due to J-mixing, $\sim 1/5000$ decays are to $J_g = 3$. This can be repumped to $J_g = 1$ via a laser tuned to the P_3 transition, denoted $\mathcal{L}_{00}^{P3}$. (c) One of several possible optical cycling schemes closed at the level of $\sim 10^4$ photon scatters. The resolved HF structure of the excited state allows for repumping excited vibrational levels through $v_e = 0$.

Bandpass interference filters centered at the wavelengths corresponding to the $B(0) \to X(0\text{–}6)$ transitions are placed before the "signal" PMT (above the vacuum chamber) to isolate fluorescence from the different vibrational bands. A second "normalization" PMT (below the chamber) contains only $271.7\,\mathrm{nm}$ interference filters and is used to measure fluorescence from the main transition $(B(0) \to X(0))$ at all times. This allows us to eliminate fluctuations in laser and molecular beam intensity from our measurements. Accounting for the small ($4\,\%$) relative quantum efficiency variation of the PMT over the range of wavelengths $271\text{–}294\,\mathrm{nm}$ does not significantly alter the branching fraction results. To avoid saturation problems with the photon counting, we limit the average number of photons collected by either PMT to be < 1 per laser pulse.

To measure a particular branching ratio we alternate between the corresponding filters, and count photons. Normalized signals are formed for each filter by subtracting the off-resonance background, normalizing with the calibration signal, and taking into account the filter transmission. The branching ratio is then formed by tak-

ing the ratio of the two normalized signals. Measurement of the ratio b_{02}/b_{00} is accomplished with a modest molecular beam flux by dividing the fluorescence signals when alternately filtering for $B(0) \to X(2)$ and $B(0) \to X(0)$. However, the small rate of the decay to $v_g \neq 0, 2$ requires higher molecular beam fluxes to achieve adequate statistical precision. To avoid saturating the normalization PMT from these larger fluorescence signals, additional attenuating filter are added. To avoid saturating the signal detector at these higher fluxes, all branching fractions b_{0v} for $v_g \neq 0, 2$ are measured by comparing the normalized signal for $B(0) \to X(v_g)$ to that of $B(0) \to X(2)$. Their measured ratio is then multiplied by b_{02} as measured above to determine b_{0v_g}. The attenuation on the normalization transition is chosen so that the statistical significance of the measurement remains dominated by the number of photons counted in the signal detector.

We calculate the experimental branching fractions displayed in Table V using the assumption that the measured branching fractions account for all of the significant vibrational branches from $v_e = 0$. It is worth noting that the uncertainty associated with b_{02} is larger than that quoted in our earlier publication [9]. The increased uncertainty is due to the identification of a systematic error associated with a changing amount of light reflected into the normalization PMT when the interference filter in the signal PMT is switched between monitoring the $v_g = 0$ and $v_g = 2$ transitions. This effect was likely also present in our earlier measurement.

D. Optical Cycling Schemes

We now examine a few specific, useful examples of optical cycling $\left| X^1\Sigma^+, J_g \right\rangle \to \left| B^3\Pi_1, \tilde{J}, F_1, F, P = f \right\rangle$ (which we abbreviate below as $\left| J_g \right\rangle \to \left| \tilde{J}, F_1, F \right\rangle$). First consider $\left| 1 \right\rangle \to \left| 1, 1/2, 0 \right\rangle$ (Fig. 5a). As there are no other $F = 0$ states, the upper state of this transition is unmixed and all quantum numbers are exact to a very high extent (Table IV). Electric dipole and parity selection rules then dictate that the excited state can only decay to $J_g = 1$.

Now consider $\left| 1 \right\rangle \to \left| 1, 1/2, 1 \right\rangle$ (Fig. 5b). This transition may be of interest in applications where a high photon scattering rate is desirable, as the higher excited state degeneracy $2F + 1$ is expected to allow for roughly $3\times$ higher photon scattering rate than the case $\left| 1 \right\rangle \to \left| 1, 1/2, 0 \right\rangle$ [25, 26]. However, the $\left| 1, 1/2, 1 \right\rangle$ excited state has $|0.0180|^2 \simeq 3 \times 10^{-4}$ fractional $J = 2$ character (Table IV). Decays from $J = 2$ go to the desired $J_g = 1$ (2/5 of the time) or to $J_g = 3$ (3/5 of the time). Hence, only $1/r_{13} \simeq 5000$ photons can be scattered before molecules are lost to the uncoupled $J_g = 3$ state. This loss is inconsequential for molecule detection applications, but is unacceptable for laser slowing and cooling. This population could be recovered by repumping $J_g = 3$ with an additional laser tuned to the $\left| 3 \right\rangle \to \left| 2, 3/2, 1, e \right\rangle$ transition. In this case, all electric dipole decay paths to

$v_g = 0$ would again be optically coupled.

Several possible optical cycling schemes exist which are closed to $\sim 10^4$ photon scatters, sufficient for laser slowing or trapping. We present one such scheme in Fig. 5c. The main cycling transition is $\left| 1 \right\rangle \to \left| 1, 1/2, 0 \right\rangle$ to minimize rotational branching. Lasers $\mathcal{L}_{v_g v_e}$ (corresponding to the transition $X(v_g) \to B(v_e)$) may be added to the optical cycle in order of decreasing importance ($\mathcal{L}_{00}$, $\mathcal{L}_{20}$, $\mathcal{L}_{40}$, $\mathcal{L}_{10}$), until the system is sufficiently closed for the intended application. The resolved excited state HF structure allows the three strongest off-diagonal vibronic decays to be repumped through $v_e = 0$ to take advantage of the near-unity b_{00} branching fraction. We calculate that with only the $\mathcal{L}_{00}$ laser, ~ 100 optical cycles may be achieved before molecules decay into a higher vibrational level. This should be sufficient for high-efficiency detection. The addition of one repump laser $\mathcal{L}_{20}$ should be sufficient to achieve transverse cooling (closed to ~ 3600 cycles). All four lasers shown in Fig. 5c would be necessary to achieve laser slowing or trapping. In this scheme, we expect to scatter $\sim 10^4$ photons before decaying to unpumped levels.

VI. CONCLUSIONS

In addition to spectroscopically identifying the Q_1 cycling transition of TlF, we have characterized the HF structure of the $B^3\Pi_1$ state. Of particular note is the large magnetic HF interaction of the Tl nuclear spin. With the exception of the lowest rotational and HF sublevel, the HF interactions significantly mix neighboring rotational levels of the B state, and lead to additional rotational branching.

TlF appears to be an excellent molecule for optical cycling. In particular, rotational and vibrational branching fractions presented here indicate ~ 100 optical cycles may be achieved using a single laser. Efficient detection with a single laser should be possible in a symmetry violation measurement using TlF. In addition, laser cooling and trapping should be feasible with four or fewer lasers.

While the measurements presented here show that the $X \to B$ system of TlF should allow for highly closed optical cycling, a number of considerations should be accounted for when choosing an appropriate cycling scheme in order to achieve a high photon scattering rate. We plan to detail these considerations in a future paper.

APPENDICES

A. Vibrational Branching Further Details

Here we offer a few important details relevant to the branching ratio measurements of Section V C. We use a number of interference filters to isolate fluorescence from individual vibronic bands. Table VI provides further details on the filters used to monitor each transition. The phototube used in these measurements (Hamamatsu R4632) has a multialkali photocathode. Its photocathode quantum efficiency varies by less that 1% over the wavelength range of our measurements and has no significant effect on our reported branching fractions.

B. Racah Algebra Identities

Here we provide a number of useful identities and their equation numbers in Ref. [27]. In the following, j_1 and j_2 are general angular momenta which couple to form angular momentum j_{12}. Rank-k tensor operators $T^k(\boldsymbol{A_1})$ and $T^k(\boldsymbol{A_2})$ act on j_1 and j_2, respectively. Tensors are represented in the spherical basis, with index p (q) for the lab frame (molecule-fixed frame) coordinate system.

Transformation from molecule-fixed frame to lab frame:

$$
\begin{aligned}
T_q^k(\boldsymbol{A}) &= \sum_p \mathscr{D}_{pq}^{(k)}(\omega) T_p^k(\boldsymbol{A}) \\
&= \sum_p (-1)^{p-q} \mathscr{D}_{-p-q}^{(k)}(\omega)^* T_p^k(\boldsymbol{A}).
\end{aligned} \quad (5.144)
$$

Scalar product of two tensor operators:

$$
\begin{aligned}
&\langle j_1, j_2, j_{12}, m | T^k(\boldsymbol{A_1}) \cdot T^k(\boldsymbol{A_2}) | j_1', j_2', j_{12}', m' \rangle \\
&= (-1)^{j_1' + j_{12} + j_2} \delta_{j_{12}, j_{12}'} \delta_{m, m'} \begin{Bmatrix} j_2' & j_1' & j_{12} \\ j_1 & j_2 & k \end{Bmatrix} \quad (5.173) \\
&\quad \times \langle j_1 || T^k(\boldsymbol{A_1}) || j_1' \rangle \langle j_2 || T^k(\boldsymbol{A_2}) || j_2' \rangle.
\end{aligned}
$$

Spectator Theorem:

$$
\begin{aligned}
&\langle j_1, j_2, j_{12} || T^k(\boldsymbol{A_1}) || j_1', j_2', j_{12}' \rangle \\
&= (-1)^{j_{12}' + j_1 + k + j_2} \delta_{j_2, j_2'} \sqrt{(2j_{12} + 1)(2j_{12}' + 1)} \\
&\quad \times \begin{Bmatrix} j_1' & j_{12}' & j_2 \\ j_{12} & j_1 & k \end{Bmatrix} \langle j_1 || T^k(\boldsymbol{A_1}) || j_1' \rangle.
\end{aligned}
$$
$$(5.174)$$

Reduced matrix element of a rank-1 tensor operator:

$$
\langle j_1 || T^1(\boldsymbol{A_1}) || j_1' \rangle = \delta_{j_1, j_1'} \sqrt{j_1(j_1 + 1)(2j_1 + 1)}. \quad (5.179)
$$

Reduced matrix element of the partially reduced Wigner rotation matrix:

$$
\begin{aligned}
&\langle J, \Omega || \mathscr{D}_{\cdot, q}^{(k)}(\omega)^* || J', \Omega' \rangle \\
&= (-1)^{J-\Omega} \sqrt{(2J+1)(2J'+1)} \begin{pmatrix} J & k & J' \\ -\Omega & q & \Omega' \end{pmatrix}.
\end{aligned}
$$
$$(5.186)$$

C. Evaluating Matrix Elements

Here we derive the HF matrix elements given in Section III. We have found references [16, 17, 27, 28] helpful in understanding which terms are likely important in the HF structure Hamiltonian. Because Ref. [27] contains all necessary fomulae for Racah algebra for diatomic molecules, we use the short-hand $\underset{(x.xx)}{=}$ for "is equivalent by Ref. [27] Eq. (x.xx)".

We begin by rotating the operator of Equation 4 into the lab frame:

$$
\langle J, \Omega, F_1, F, m | T_{q=0}^1(\boldsymbol{I}) | J', \Omega', F_1', F, m \rangle \underset{(5.144)}{=}
$$
$$
\sum_p (-1)^p \langle J, \Omega, F_1, F, m | \mathscr{D}_{-p,0}^{(1)}(\omega)^* T_p^1(\boldsymbol{I}) | J', \Omega', F_1, F, m \rangle
$$
$$(14)$$

For $I = I_1$,

$$
\underset{(5.173)}{=} (-1)^{J' + F_1 + I_1} \delta_{F_1, F_1'} \begin{Bmatrix} I_1 & J' & F_1 \\ J & I_1 & 1 \end{Bmatrix}
$$
$$
\times \langle J, \Omega || \mathscr{D}_{\cdot, 0}^{(1)}(\omega)^* || J', \Omega' \rangle \langle I_1 || T^1(\boldsymbol{I_1}) || I_1 \rangle
$$
$$
\underset{\substack{(5.179) \\ (5.186)}}{=} (-1)^{J + J' + F_1 + I_1 - \Omega} \delta_{F_1, F_1'} \qquad (15)
$$
$$
\times \begin{Bmatrix} I_1 & J' & F_1 \\ J & I_1 & 1 \end{Bmatrix} \begin{pmatrix} J & 1 & J' \\ -\Omega & 0 & \Omega' \end{pmatrix}
$$
$$
\times [(2J + 1)(2J' + 1) I_1(I_1 + 1)(2I_1 + 1)]^{1/2},
$$

which matches Ref. [16] Eq. (6). Note that when employing (5.173) to get the first line of Eq. 15, both the Wigner rotation matrix $\mathscr{D}$ and $T^1(\boldsymbol{I_1})$ are being reduced in the lab frame (indexed by p). Specifically, the term $\langle J, \Omega || \mathscr{D}_{\cdot, 0}^{(1)}(\omega)^* || J', \Omega' \rangle$ is the partially reduced Wigner rotation matrix (reduced in the lab frame, but not the molecule-fixed frame), whose value is given by Ref. [27] Eq. 5.186. For $I = I_2$, Eq. 14 yields

$$
\underset{(5.173)}{=} (-1)^{F_1' + F + I_2} \begin{Bmatrix} I_2 & F_1' & F \\ F_1 & I_2 & 1 \end{Bmatrix}
$$
$$
\times \langle J, \Omega, F_1 || \mathscr{D}_{\cdot, 0}^{(1)}(\omega)^* || J', \Omega', F_1' \rangle \langle I_2 || T^1(\boldsymbol{I_2}) || I_2 \rangle
$$
$$
\underset{(5.174)}{=} (-1)^{F_1' + F + I_2} \begin{Bmatrix} I_2 & F_1' & F \\ F_1 & I_2 & 1 \end{Bmatrix}
$$
$$
\times (-1)^{F_1' + J + 1 + I_1} [(2F_1 + 1)(2F_1' + 1)]^{1/2} \begin{Bmatrix} J' & F_1' & I_1 \\ F_1 & J & 1 \end{Bmatrix}
$$
$$
\times \langle J, \Omega || \mathscr{D}_{\cdot, 0}^{(1)}(\omega)^* || J', \Omega' \rangle \langle I_2 || T^1(\boldsymbol{I_2}) || I_2 \rangle
$$
$$
\underset{\substack{(5.179) \\ (5.186)}}{=} (-1)^{2F_1' + F + 2J + 1 + I_1 + I_2 - \Omega}
$$
$$
\times \begin{Bmatrix} I_2 & F_1' & F \\ F_1 & I_2 & 1 \end{Bmatrix} \begin{Bmatrix} J' & F_1' & I_1 \\ F_1 & J & 1 \end{Bmatrix} \begin{pmatrix} J & 1 & J' \\ -\Omega & 0 & \Omega' \end{pmatrix}
$$
$$
\times [(2F_1 + 1)(2F_1' + 1)(2J + 1)(2J' + 1)
$$
$$
\times I_2(I_2 + 1)(2I_2 + 1)]^{1/2},
$$
$$(16)$$

which again matches Ref. [16] Eq. (6).

$B(0) \to X(v_g)$	λ_{0v_g}	Part Number	λ_{peak}	FWHM	$T(\lambda_{0v_g})$	$T(271.7\,\text{nm})$	b_{BG}
$v_g = 0$	271.7 nm	R214-01	271.8 nm	10.3 nm	0.179	–	–
		R214-02	271.3 nm	10.1 nm	0.170	–	–
		neutral density	–	–	0.135	–	–
$v_g = 1$	275.3 nm	T144-02	275.4 nm	1.3 nm	0.141	$8 \cdot 10^{-5}$	
		R088-01	275.3 nm	1.3 nm	0.138	$8 \cdot 10^{-5}$	$3 \cdot 10^{-7}$
$v_g = 2$	278.8 nm	S078-02	279.3 nm	2 nm	0.099	$2 \cdot 10^{-5}$	$2 \cdot 10^{-4}$
$v_g = 3$	282.5 nm	T236-04	282.7 nm	1.4 nm	0.129	$3 \cdot 10^{-6}$	
		T236-05	282.8 nm	1.5 nm	0.124	$1 \cdot 10^{-6}$	$2 \cdot 10^{-10}$
$v_g = 4$	286.2 nm	T338-01	286.5 nm	1.6 nm	0.114	$1 \cdot 10^{-6}$	
		T335-10	290.9 nm	10.7 nm	0.110	$5 \cdot 10^{-3}$	$4 \cdot 10^{-7}$
$v_g = 5$	290.0 nm	T338-02	290.3 nm	1.6 nm	0.110	$2 \cdot 10^{-6}$	
		T335-10	290.9 nm	10.7 nm	0.178	$5 \cdot 10^{-3}$	$8 \cdot 10^{-7}$
$v_g = 6$	293.8 nm	T335-14	297.9 nm	10.8 nm	0.117	$7 \cdot 10^{-4}$	
		T335-15	298.7 nm	11.6 nm	0.100	$9 \cdot 10^{-4}$	$5 \cdot 10^{-5}$
$v_g = 7$	297.6 nm	T335-14	297.9 nm	10.8 nm	0.149	$7 \cdot 10^{-4}$	
		T335-15	298.7 nm	11.6 nm	0.149	$9 \cdot 10^{-4}$	$3 \cdot 10^{-5}$
$v_g = 8$	301.4 nm	T335-14	297.9 nm	10.8 nm	0.110	$7 \cdot 10^{-4}$	
		T335-15	298.7 nm	11.6 nm	0.122	$9 \cdot 10^{-4}$	$5 \cdot 10^{-5}$

TABLE VI. Properties of bandpass filters used in vibrational branching measurement: part numbers (Andover), bandwidths, and transmission T. Measurements of peak transmission wavelength λ_{peak}, transmission full width at half maximum (FWHM), and $T(\lambda_{0v_g})$ were performed by the manufacturer. Measurements of $T(271.7\,\text{nm})$ were performed using our laser source and power meter. A spatial filter before the phototube restricts the light emitted from the molecular fluorescence region to angles of incidence less than $2\,^\circ$ on the interference filters. Including this range of angles, we measure the uncertainty in $T(\lambda_{0v_g})$ for the interference filters to be less than $1.5\,\%$. Uncertainty in $T(\lambda_{0v_g})$ for the neutral density filter is 1%. For each of the weak transitions, both of the listed filters are used in our measurements in order to minimize leakage. From the residual transmission at $271.7\,\text{nm}$, we calculate the expected background to the branching fraction b_{BG}. In all cases except for b_{06+}, the expected background b_{BG} is negligible compared to the values b_{0v_g} given in Table V. For b_{06+}, the use of relatively broadband interference filters leads to significant simultaneous transmission of wavelengths corresponding to decays to $v_g = 6$, 7, and 8. The limit on b_{06+} in Table V reflects our experimental sensitivity to decays to these three levels, assuming decays to $v_g \geq 9$ are negligible.

The nuclear spin-rotation matrix elements can be written as follows. For $I = I_1$:

$$
\begin{aligned}
&\langle J, \Omega, F_1, F, m | T^1(\boldsymbol{I_1}) \cdot T^1(\boldsymbol{J}) | J', \Omega', F_1', F, m \rangle \\
&\underset{(5.173)}{=} (-1)^{J'+F_1+I_1} \delta_{F_1, F_1'} \begin{Bmatrix} I_1 & J' & F_1 \\ J & I_1 & 1 \end{Bmatrix} \\
&\quad \times \langle J || T^1(\boldsymbol{J}) || J' \rangle \, \langle I_1 || T^1(\boldsymbol{I_1}) || I_1 \rangle \\
&\underset{(5.179)}{=} (-1)^{J+F_1+I_1} \delta_{F_1, F_1'} \delta_{J,J'} \begin{Bmatrix} I_1 & J & F_1 \\ J & I_1 & 1 \end{Bmatrix} \\
&\quad \times [(J(J+1)(2J+1)I_1(I_1+1)(2I_1)+1)]^{1/2}.
\end{aligned}
\tag{17}
$$

Now for $I = I_2$:

$$
\begin{aligned}
&\langle J, \Omega, F_1, F, m | T^1(\boldsymbol{I_2}) \cdot T^1(\boldsymbol{J}) | J', \Omega', F_1', F, m \rangle \\
&\underset{(5.173)}{=} (-1)^{F_1'+F+I_2} \begin{Bmatrix} I_2 & F_1' & F \\ F_1 & I_2 & 1 \end{Bmatrix} \\
&\quad \times \langle J, I_1, F_1 || T^1(\boldsymbol{J}) || J', I_1, F_1' \rangle \, \langle I_2 || T^1(\boldsymbol{I_2}) || I_2 \rangle \\
&\underset{(5.174)}{=} (-1)^{F_1'+F+I_2} \begin{Bmatrix} I_2 & F_1' & F \\ F_1 & I_2 & 1 \end{Bmatrix} \\
&\quad \times (-1)^{F_1'+J+I_1+1} [(2F_1+1)(2F_1')]^{1/2} \begin{Bmatrix} J' & F_1' & I_1 \\ F_1 & J & 1 \end{Bmatrix} \\
&\quad \times \langle J || T^1(\boldsymbol{J}) || J' \rangle \, \langle I_2 || T^1(\boldsymbol{I_2}) || I_2 \rangle \\
&\underset{(5.179)}{=} (-1)^{2F_1'+F+J+I_1+I_2+1} \delta_{J,J'} \\
&\quad \times \begin{Bmatrix} I_2 & F_1' & F \\ F_1 & I_2 & 1 \end{Bmatrix} \begin{Bmatrix} J' & F_1' & I_1 \\ F_1 & J & 1 \end{Bmatrix} \\
&\quad \times \big[(2F_1+1)(2F_1'+1)J(J+1)(2J+1) \\
&\quad\quad \times I_2(I_2+1)(2I_2+1) \big]^{1/2}.
\end{aligned}
\tag{18}
$$

Results 17 and 18 match Ref. [27] (8.290) and (8.291), respectively, as well as Ref. [28] (5). However, Eq. 17 differs from Ref. [16] by a factor of $[J(J+1)(2J+1)]^{1/2}$.

D. Full Q Branch Spectrum

In Fig. 6, we include the full Q branch spectrum of the $X \to B$ transition in TlF. Line centers predicted by the best-fit rotational constants in Table III are in excellent agreement with the observed spectrum.
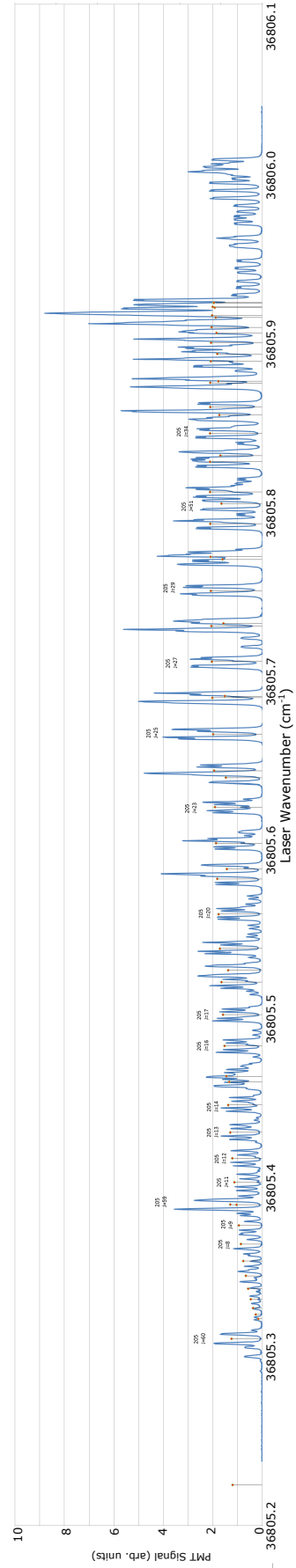

FIG. 6. PMT signal vs laser frequency in the thermal beam showing all identified Q branch lines. Drop lines indicate calculated line centers from best-fit rotational constants (Table III).

[1] E. A. Hinds and P. G. H. Sandars, Phys. Rev. A **21**, 480 (1980).

[2] D. A. Wilkening, N. F. Ramsey, and D. J. Larson, Phys. Rev. A **29**, 425 (1984).

[3] D. Cho, K. Sangster, and E. A. Hinds, Phys. Rev. A **44**, 2783 (1991).

[4] I. B. Khriplovich and S. K. Lamoreaux, *CP violation without strangeness: electric dipole moments of particles, atomics, and molecules* (Springer-Verlag, 1997).

[5] L. I. Schiff, Phys. Rev. **132**, 2194 (1963).

[6] E. S. Shuman, J. F. Barry, D. R. Glenn, and D. DeMille, Phys. Rev. Lett. **103**, 223001 (2009).

[7] E. S. Shuman, J. F. Barry, and D. DeMille, Nature **467**, 820 (2010).

[8] J. F. Barry, D. J. McCarron, E. N. Norrgard, M. H. Steinecker, and D. DeMille, Nature **512**, 286 (2014).

[9] L. R. Hunter, S. K. Peck, A. S. Greenspon, S. S. Alam, and D. DeMille, Phys. Rev. A **85**, 012511 (2012).

[10] J. Hoeft, F. J. Lovas, E. Tiemann, and T. Törring, Zeitschrift Naturforschung Teil A **25**, 1029 (1970).

[11] U. Wolf and E. Tiemann, Chemical Physics Letters **133**, 116 (1987).

[12] J. F. Barry, E. S. Shuman, and D. DeMille, Phys. Chem. Chem. Phys. **13**, 18936 (2011).

[13] D. R. Lide, *CRC Handbook of Chemistry and Physics*, 77th ed. (CRC Press, 1997).

[14] G. Herzberg, *Molecular Spectra and Molecular Structure: I. Spectra of Diatomic Molecules, 2nd Ed.* (D. Van Nostrand Company, Inc, New York, 1950).

[15] K. Balasubramanian, The Journal of Chemical Physics **82**, 3741 (1985).

[16] T. Okabayashi, T. Kurahara, E. Y. Okabayashi, and M. Tanimoto, The Journal of Chemical Physics **136**, 174311 (2012).

[17] T. Okabayashi and M. Tanimoto, Journal of Molecular Spectroscopy **221**, 149 (2003).

[18] E. Tiemann, Molecular Physics **65**, 359 (1988).

[19] C. Townes and A. L. Schawlow, *Microwave Spectroscopy* (McGraw-Hill, New York, 1955).

[20] A.-M. Mårtensson-Pendrill, Phys. Rev. Lett. **74**, 2184 (1995).

[21] D. S. Richardson, R. N. Lyman, and P. K. Majumder, Phys. Rev. A **62**, 012510 (2000).

[22] H. Knöckel and E. Tiemann, Chemical Physics Letters **104**, 83 (1984).

[23] J. F. Barry, E. S. Shuman, E. B. Norrgard, and D. DeMille, Phys. Rev. Lett. **108**, 103002 (2012).

[24] G. J. Feldman and R. D. Cousins, (1997), arXiv:physics:9711021.

[25] E. B. Norrgard, D. J. McCarron, M. H. Steinecker, M. R. Tarbutt, and D. DeMille, Phys. Rev. Lett. **116**, 063004 (2016).

[26] E. B. Norrgard, *Magneto-optical trapping of diatomic molecules*, Ph.D. thesis, Yale University (2016).

[27] J. M. Brown and A. Carrington, *Rotational spectroscopy of diatomic molecules* (Cambridge Univ. Press, 2003).

[28] B. J. Knurr, E. K. Butler, and T. D. Varberg, The Journal of Physical Chemistry A **113**, 13428 (2009).